Equilibrium fluctuations of DNA plectonemes

Enrico Skoruppa and Enrico Carlon
Soft Matter and Biophysics, Department of Physics and Astronomy, KU Leuven, Leuven, Belgium

(Received 17 May 2022; accepted 5 August 2022; published 26 August 2022)

Plectonemes are intertwined helically looped domains which form when a DNA molecule is supercoiled, i.e., over- or underwound. They are ubiquitous in cellular DNA, and their physical properties have attracted significant interest both from the experimental side and from the modeling side. In this paper, we investigate fluctuations of the end-point distance z of supercoiled linear DNA molecules subject to external stretching forces. Our analysis is based on a two-phase model, which describes the supercoiled DNA as composed of a stretched phase and a plectonemic phase. A variety of mechanisms are found to contribute to extension fluctuations, characterized by the variance $\langle \Delta z^2 \rangle$. We find the dominant contribution to $\langle \Delta z^2 \rangle$ to originate from phase-exchange fluctuations, the transient shrinking and expansion of plectonemes, which is accompanied by an exchange of molecular length between the two phases. We perform Monte Carlo simulations of the twistable wormlike chain and analyze the fluctuation of various quantities, the results of which are found to agree with the two-phase model predictions. Furthermore, we show that the extension and its variance at high forces are very well captured by the two-phase model, provided that one goes beyond quadratic approximations.

DOI: 10.1103/PhysRevE.106.024412

I. INTRODUCTION

The readout of genetic information stored in DNA is known to be regulated by physical strains such as bending and twisting. A particular form of such strains arises if DNA contained in topologically insulated domains is maintained in an under- or overwound state. While the topological linking number Lk of the two individual single strands remains conserved, Lk partitions into the geometric properties twist and writhe $\mathrm{Lk} = \mathrm{Tw} + \mathrm{Wr}$ [1–3], where Tw represents the accumulative local wrapping of the two backbones and writhe quantifies the degree of coiling exhibited by the helical centerline curve. Plectonemic supercoils, which are helically intertwined regions [see Fig. 1(a)], appear in DNA if the linking number exceeds some threshold value. Supercoiling is known to be prevalent both in bacterial plasmids and in eukaryotic chromosomes, which are organized in topological domains [4,5]. These coils contribute to a multitude of physiological processes, such as DNA compaction [6], facilitation of DNA bridging via restriction enzymes [7–10], control of chromatin accessibility [4,5], and the regulation of gene expression [11–13].

Owing to its biological relevance, DNA supercoiling has attracted significant interest for a long time, both from the experimental side and from the modeling side [14–34]. The properties of DNA supercoils can be probed *in vitro* by means of single-molecule experiments such as magnetic tweezers (MT) [35,36]. In these experiments, a linear DNA molecule is attached to a solid surface at one end and to a paramagnetic bead at the other end [Fig. 1(a)]. A magnetic field is used to apply a stretching force f and to control the total torsional strain of the molecule by restricting the rotation of the bead. In torsionally relaxed DNA, the two strands wind around each other Lk_0 times, corresponding to one turn every 10.5 base pairs (bp) (the linking number of torsionally relaxed DNA). Rotating the bead away from the relaxed state induces excess linking number $\Delta\mathrm{Lk} = \mathrm{Lk} - \mathrm{Lk}_0 \neq 0$, which can be either positive or negative for overwound or underwound DNA, respectively. It is convenient to define the supercoiling density $\sigma = \Delta\mathrm{Lk}/\mathrm{Lk}_0$, which is an intensive quantity, independent of the total length of the molecule. Starting from a torsionally relaxed state ($\sigma = 0$) under an applied stretching force f, one can gradually increase σ. At a certain threshold $\sigma = \sigma_s$ the molecule buckles: Plectonemic supercoils appear, and the end-to-end distance z is reduced [Fig. 1(a)]. Upon further increase of σ, the plectoneme grows at the cost of the stretched part of the molecule.

Our analysis of linear DNA supercoiling is based on the two-phase model [14,15], which describes the DNA molecule as being composed of a stretched phase and a plectonemic phase, each with distinct free energies; see Fig. 1(b). We treat DNA as a homogeneous polymer neglecting sequence-dependent effects, which are expected to be negligible for the long molecules [of the order of kilobase pairs (kbp)] used in the considered experiments. In the homogeneous two-phase model, buckling is analogous to a thermodynamic first-order transition. While typical theoretical and experimental work on supercoiling in MT focuses on the average signal $\langle z \rangle$, we discuss the fluctuations in the extension z characterized by the variance $\langle \Delta z^2 \rangle$. Recent experiments show that a change in $\langle \Delta z^2 \rangle$ can be associated with the formation of topological domains induced by proteins that bridge across different sites of DNA [37]. In addition, insights into equilibrium fluctuations can shed light on the rich dynamics of plectonemes [25].

The aim of this work is to investigate the properties and origin of fluctuations in linear supercoiled DNA. We first

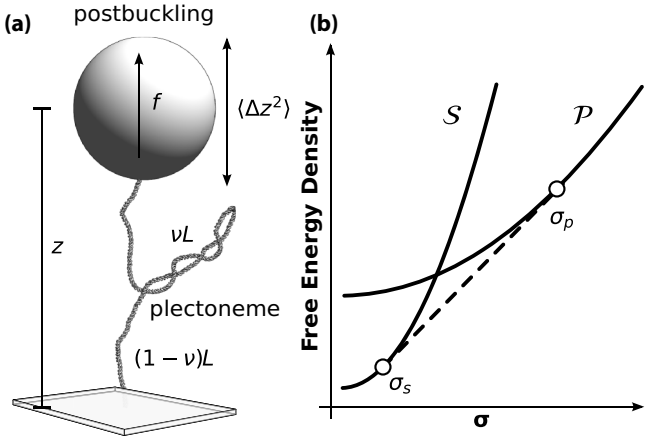

FIG. 1. (a) Example of plectoneme supercoil formation as induced in MT experiments by rotation of the end point of a DNA molecule stretched by a linear force f. At postbuckling, the molecule phase separates into a stretched phase and a plectonemic phase. The total length of the molecule L is partitioned between the two phases, and $0 \leqslant \nu \leqslant 1$ indicates the fraction of length in the stretched phase. (b) Sketch of free energies per unit length of the stretched and plectonemic phases' free energies $\mathcal{S}$ and $\mathcal{P}$, respectively, as introduced in the two-phase model of linear supercoiled DNA buckling [14,15]. The dashed line indicates the double-tangent construction.

discuss the two-state model of DNA supercoiling and extend it to the analysis of fluctuations. We show the leading contribution to $\langle \Delta z^2 \rangle$ to be associated with *phase-exchange fluctuations*, i.e., the transient transfer of contour length between the plectonemic phase and the stretched phase. Moreover, our analysis highlights that the extension variance is a lot more sensitive to the properties of the plectonemic phase than the average extension. It is therefore an excellent quantity to be used for the assessment of plectoneme free-energy models [38,39]. Our theoretical analysis is supported by numerical results obtained by extensive Monte Carlo simulations, which are in good agreement with the two-phase model predictions, both for average quantities and for their fluctuations.

II. FLUCTUATIONS IN EXTENSION FROM THE TWO-PHASE MODEL

In order to describe the phenomenology of DNA supercoiling, we follow the commonly employed two-phase model approach that partitions a DNA molecule of length L, stretched by a force f and subject to supercoil density σ, into two separate phases [14,15]. A fraction ν of the entire molecular length is assumed to be in the stretched phase [Fig. 1(a)] maintained at supercoil density ϕ, while the remainder length is in the plectonemic phase with supercoil density ψ. As the total linking number in the system is fixed by the amount of turns applied to the bead (i.e., σ is fixed), fluctuations of the quantities ν, ϕ, and ψ are constrained to the requirement for the total linking density to equal the sum of the contributions within the two domains: $\sigma = \nu\phi + (1-\nu)\psi$. In the following, we will regard ν and ϕ as independent variables, which fixes ψ to

$$\psi = \frac{\sigma - \nu\phi}{1-\nu}. \tag{1}$$

Following Ref. [15], we consider the free energies per unit length of the stretched and plectonemic phases $\mathcal{S}(\phi, f)$ and $\mathcal{P}(\psi)$, respectively, such that the combined free energy per unit length becomes the linear combination

$$\mathcal{F}(\phi, \nu, f) = \nu\mathcal{S}(\phi, f) + (1-\nu)\mathcal{P}(\psi). \tag{2}$$

No explicit force dependence is assumed for $\mathcal{P}(\psi)$ as plectonemes do not contribute to the end-to-end extension. While specific choices of these free energies will be discussed further on, for the time being we will explore general properties. To reproduce the observed phenomenology, we only require the free energies to be convex in σ and $\mathcal{S}(\sigma, f) < \mathcal{P}(\sigma)$ for small σ, while $\mathcal{S}(\sigma, f) > \mathcal{P}(\sigma)$ for sufficiently large σ, reflecting the absence of plectonemes at small supercoiling densities and their proliferation at large σ.

The partition function of a molecule of total length L subject to a stretching force f, fixed σ, and large L is then given by

$$Z(\sigma, f, L) = \int_0^1 d\nu \int_{-\infty}^{+\infty} d\phi \; e^{-\beta L \mathcal{F}(\phi,\nu,f)} \approx e^{-\beta L \widetilde{\mathcal{F}}(\sigma,f)}, \tag{3}$$

where the free energy in the saddle-point approximation

$$\widetilde{\mathcal{F}}(\sigma, f) \equiv \min_{\{\phi,\nu\}} \left[\nu\mathcal{S}(\phi, f) + (1-\nu)\mathcal{P}\left(\frac{\sigma - \phi\nu}{1-\nu}\right)\right] \tag{4}$$

is obtained from the condition of vanishing derivatives $\partial\mathcal{F}/\partial\phi = 0$ and $\partial\mathcal{F}/\partial\nu = 0$; see Ref. [15]. This minimization leads to a double-tangent construction [see Fig. 1(b)]

$$\widetilde{\mathcal{F}}(\sigma, f) = \begin{cases} \mathcal{S}(\sigma, f) & 0 \leqslant \sigma \leqslant \sigma_s \\ \frac{(\sigma_p - \sigma)\mathcal{S}(\sigma_s, f) + (\sigma - \sigma_s)\mathcal{P}(\sigma_p)}{\sigma_p - \sigma_s} & \sigma_s \leqslant \sigma \leqslant \sigma_p \\ \mathcal{P}(\sigma) & \sigma \geqslant \sigma_p. \end{cases} \tag{5}$$

Within the range $0 \leqslant \sigma \leqslant \sigma_s$ the minimum corresponds to a pure stretched phase, i.e., $\nu = 1$ and $\phi = \sigma$, commonly referred to as the prebuckling regime. For $\sigma_s \leqslant \sigma \leqslant \sigma_p$, the free energy is a linear combination of stretched phase and plectoneme phase free energies, with a fraction

$$\nu_s = \langle \nu \rangle = \frac{\sigma_p - \sigma}{\sigma_p - \sigma_s}, \tag{6}$$

of molecular contour length contained in the stretched phase. This regime is known as the postbuckling regime, with σ_s denoting the buckling transition or buckling point. Finally, for $\sigma > \sigma_p$, corresponding to $\nu = 0$ and $\psi = \sigma$, the plectonemic phase fully engulfs the molecule, reducing the end-point extension to zero. The two-phase model describes buckling as a first-order phase transition [15]. For $\sigma_s \leqslant \sigma \leqslant \sigma_p$ the molecule separates into stretched and plectonemic domains with *average* supercoil densities σ_s and σ_p in full analogy to a fluid, which phase separates into a liquid and a vapor phase with distinct particle densities n_L and n_V. We emphasize that σ_s and σ_p are average supercoil densities. At equilibrium, the supercoil densities (ϕ and ψ) as well as the fractional lengths

of the two phases (ν and $1-\nu$) exhibit fluctuations. It is precisely the scope of this paper to analyze the properties of these equilibrium fluctuations.

The experimentally accessible average molecular extension along the direction of the force director field is obtained from the total derivative of the free energy with respect to the force

$$\frac{\langle z\rangle}{L} = -\frac{d\widetilde{\mathcal{F}}}{df}, \tag{7}$$

while the variance is obtained by the second derivative

$$\frac{\langle \Delta z^2\rangle}{L} = -k_B T \frac{d^2\widetilde{\mathcal{F}}}{df^2}. \tag{8}$$

A. Fluctuations in ϕ, ψ, and ν

The fluctuations of the supercoiling densities ϕ and ψ as well as the fractional occupancy of the stretched phase ν in the postbuckling regime can be understood on general grounds. Taylor expansion of the free energy per unit length (2) around the minimum at σ_s and ν_s yields

$$\begin{aligned}\mathcal{F} \approx \widetilde{\mathcal{F}} + \tfrac{1}{2}[&\mathcal{F}_{\nu\nu}(\nu-\nu_s)^2 + \mathcal{F}_{\phi\phi}(\phi-\sigma_s)^2 \\ &+ 2\mathcal{F}_{\nu\phi}(\nu-\nu_s)(\phi-\sigma_s)],\end{aligned} \tag{9}$$

where $\widetilde{\mathcal{F}}$ is the minimal free energy (4) and $\mathcal{F}_{\nu\nu}$, $\mathcal{F}_{\phi\phi}$, $\mathcal{F}_{\phi\nu}$ are the second derivatives of $\mathcal{F}$ with respect to ν and ϕ. These form a 2×2 Hessian matrix, which upon inversion gives the following results for the fluctuations (for details, see Appendix A):

$$\langle \Delta\nu^2\rangle = \frac{k_B T}{L(\sigma_p-\sigma_s)^2}\left(\frac{1-\nu_s}{\mathcal{P}_{\psi\psi}} + \frac{\nu_s}{\mathcal{S}_{\phi\phi}}\right), \tag{10}$$

$$\langle \Delta\phi^2\rangle = \frac{k_B T}{L\nu_s \mathcal{S}_{\phi\phi}}, \tag{11}$$

$$\langle \Delta\nu\Delta\phi\rangle = \frac{k_B T}{L(\sigma_p-\sigma_s)\mathcal{S}_{\phi\phi}}, \tag{12}$$

where $\Delta\nu \equiv \nu-\nu_s$, $\Delta\phi \equiv \phi-\sigma_s$ and where $\mathcal{S}_{\phi\phi}$ and $\mathcal{P}_{\psi\psi}$ are the second derivatives of the free energies of the stretched and plectonemic phases with respect to the corresponding supercoiling densities. Evaluation at $\phi=\sigma_s$ and $\psi=\sigma_p$ is implied. Analogously, the plectoneme supercoiling density fluctuates as

$$\langle \Delta\psi^2\rangle = \frac{k_B T}{L(1-\nu_s)\mathcal{P}_{\psi\psi}}. \tag{13}$$

The variances of the supercoiling densities ϕ and ψ are inversely proportional to the curvature of the respective free energy at the minimum, $\mathcal{S}_{\phi\phi}$ and $\mathcal{P}_{\psi\psi}$, and the average lengths of the two phases, $\nu_s L$ and $(1-\nu_s)L$. As in the postbuckling regime ν_s decreases with increasing σ [Eq. (6)], the variance of the stretched phase supercoil density $\langle\Delta\phi^2\rangle$ increases with σ. Conversely, $\langle\Delta\psi^2\rangle$ decreases with increasing σ, while the cross-correlator $\langle\Delta\nu\Delta\phi\rangle$ is independent of σ.

In the prebuckling regime $0 \leqslant \sigma < \sigma_s$, the system is in the pure stretched phase $\nu_s = 1$, such that there are no phase-exchange fluctuations $\langle\Delta\nu^2\rangle = 0$. When advancing into the postbuckling regime, the system traverses the buckling point where the variance in ν exhibits a discrete jump into nonzero fluctuations

$$\lim_{\sigma\to\sigma_s^+}\langle\Delta\nu^2\rangle - \lim_{\sigma\to\sigma_s^-}\langle\Delta\nu^2\rangle = \frac{k_B T}{L}\frac{1}{\mathcal{S}_{\phi\phi}(\sigma_p-\sigma_s)^2}. \tag{14}$$

Similarly, fluctuations in ϕ and ψ exhibit a discontinuity at the buckling point, since $\phi=\sigma$ and $\psi=0$ at prebuckling. From Eqs. (10) and (6) we find

$$\frac{d\langle\Delta\nu^2\rangle}{d\sigma} = \frac{k_B T}{L(\sigma_p-\sigma_s)^3}\frac{\mathcal{S}_{\phi\phi}-\mathcal{P}_{\psi\psi}}{\mathcal{S}_{\phi\phi}\mathcal{P}_{\psi\psi}}, \tag{15}$$

which shows that fluctuations in ν increase throughout the postbuckling regime if $\mathcal{S}_{\phi\phi} > \mathcal{P}_{\psi\psi}$ at the minimum $\phi=\sigma_s$, $\psi=\sigma_p$. This is the typical behavior of DNA, as the stretched phase is torsionally stiffer than the plectonemic phase [15].

B. Quadratic free energies

As a concrete and analytically tractable example we consider quadratic free energies for the two phases [15]

$$\mathcal{S}(\phi, f) = -g(f) + a(f)\phi^2, \tag{16}$$

$$\mathcal{P}(\psi) = b\psi^2. \tag{17}$$

While the free energy of the stretched phase of type (16) can be derived from the twistable wormlike chain (TWLC) [40], the form of the plectonemic free energy (17) is purely phenomenological. It assumes symmetry in $\pm\psi$, valid at low forces ($f < 1$ pN) where DNA exhibits near-symmetric behavior upon over- and underwinding. Equation (17) can be viewed as the lowest-order expansion of a generic $\mathcal{P}(\psi)$. As such, this form will be valid for sufficiently small supercoiling densities. For the TWLC, the coefficients g and a describing the free energy of the stretched phase are force dependent [40–42]. Since the system is assumed to be fully in the stretched phase at low supercoiling densities, we require $g > 0$ to ensure that $\mathcal{S}(0, f) < \mathcal{P}(0)$. Moreover, to have a transition from the stretched phase to the plectonemic phase, the free energy of the former has to exceed that of the latter ($\mathcal{P} < \mathcal{S}$) for sufficiently large supercoiling density, which requires $a(f) > b$ [this corresponds to $\mathcal{S}_{\phi\phi} > \mathcal{P}_{\psi\psi}$, i.e., an increase in variance with increasing σ, as per Eq. (15)].

For the free energies (16) and (17) the double-tangent construction yields the average supercoiling densities of stretched and plectonemic phases [15]

$$\langle\phi\rangle = \sigma_s = \sqrt{\frac{bg}{a(a-b)}}, \quad \langle\psi\rangle = \sigma_p = \sqrt{\frac{ag}{b(a-b)}}. \tag{18}$$

The free energy in the postbuckling regime ($\sigma_s \leqslant \sigma \leqslant \sigma_p$) assumes the form

$$\widetilde{\mathcal{F}}(\sigma, f) = -\frac{ga}{a-b} + 2\sigma\sqrt{\frac{gab}{a-b}}, \tag{19}$$

which is linear in σ and depends on f through the force dependence of g and a.

The fluctuations of Eqs. (10)–(13) take the form

$$\langle \Delta\nu^2 \rangle = \frac{k_B T \sigma}{2Lg^{3/2}} \sqrt{\frac{ab}{a-b}}, \tag{20}$$

$$\langle \Delta\phi^2 \rangle = \frac{k_B T}{2aL\nu_s}, \tag{21}$$

$$\langle \Delta\psi^2 \rangle = \frac{k_B T}{2bL(1-\nu_s)}, \tag{22}$$

$$\langle \Delta\phi \Delta\nu \rangle = \frac{k_B T}{2L} \sqrt{\frac{ab}{g(a-b)}}, \tag{23}$$

where we used (18) to express σ_s and σ_p as a function of the parameters a, b, and g in Eqs. (20) and (23). Equations (21) and (22) follow directly from the general expressions (11) and (13) using $\mathcal{S}_{\phi\phi} = 2a$ and $\mathcal{P}_{\psi\psi} = 2b$ for the second derivatives of the free-energy densities of the quadratic model. Expressions that are a function of σ instead of ν_s are easily obtained by invoking Eq. (6) with σ_p and σ_s given by (18). Note that $\langle \Delta\nu^2 \rangle$ increases with σ, as deduced from (15): The stretched phase is torsionally stiffer than the plectonemic phase ($a > b$).

While so far we have considered the asymptotic limit $L \to \infty$, one can extend the analysis to finite-length effects. For this purpose, one can start from (3) and perform the (Gaussian) integral on ϕ explicitly

$$Z(\sigma, f, L) = \int_0^1 d\nu \int_{-\infty}^{+\infty} d\phi \; e^{-\beta L \nu \mathcal{S}(\phi, f)} e^{-\beta L (1-\nu)\mathcal{P}(\psi)} = \cdots \int_0^1 d\nu \, e^{-\beta L \mathcal{G}(\nu)}, \tag{24}$$

where the dots indicate subleading terms in $1/L$. The free energy $\mathcal{G}(\nu)$ is found to be

$$\mathcal{G}(\nu) = -\nu g + \Xi(\nu)\sigma^2, \tag{25}$$

which is characterized by an effective stiffness

$$\frac{1}{\Xi(\nu)} = \frac{\nu}{a} + \frac{1-\nu}{b}, \tag{26}$$

given by the weighted harmonic mean of the stiffnesses of the stretched (a) and plectonemic (b) phases. As expected, this free energy reduces to the pure state free energies in the two extremal cases $\mathcal{G}(\nu = 1) = \mathcal{S}$ and $\mathcal{G}(\nu = 0) = \mathcal{P}$. $\mathcal{G}(\nu)$ is plotted in Fig. 2 for three different values of σ. In the postbuckling regime $\sigma_s < \sigma < \sigma_p$ the fluctuations of ν are obtained from the second derivative of $\mathcal{G}(\nu)$ calculated in ν_s from which one recovers (20). This Gaussian approximation is valid at large L and breaks down in the vicinity of the phase boundaries $\nu_s \approx 0$ and $\nu_s \approx 1$. In that case, the partition function (24) can be obtained by numerical integration.

1. Rigid rod model

To illustrate the phenomenology of extension fluctuations, we start with a simple model in which thermally activated bending fluctuations within the stretched phase are neglected. We assume that this phase consists of twistable rigid rods aligned along the direction of the force. This corresponds to setting $g(f) = f$ and $a(f) = a$ in Eq. (16), with a constant. In the prebuckling regime $0 < \sigma < \sigma_s$, one obtains the average and variance of z from differentiating $\mathcal{S}(\sigma, f)$ with respect to f. The calculation gives $\langle z \rangle = L$ and $\langle \Delta z^2 \rangle = 0$, showing that this choice of stretched phase free energy indeed represents a straight rod. In the postbuckling regime $\sigma_s < \sigma < \sigma_p$, differentiation of (19) is simple as the only force dependence in the parameters is $g = f$:

$$\frac{\langle z \rangle}{L} = -\frac{d\widetilde{\mathcal{F}}}{df} = \frac{a}{a-b} - \frac{\sigma}{\sqrt{f}} \sqrt{\frac{ab}{a-b}}. \tag{27}$$

Using (18), one can easily verify that (27) yields $\langle z \rangle = L$ for $\sigma = \sigma_s$ and that $\langle z \rangle = 0$ for $\sigma = \sigma_p$. For the variance, one obtains

$$\frac{\langle \Delta z^2 \rangle}{L} = -k_B T \frac{d^2\widetilde{\mathcal{F}}}{df^2} = \frac{k_B T \sigma}{2f^{3/2}} \sqrt{\frac{ab}{a-b}} = L\langle \Delta\nu^2 \rangle, \tag{28}$$

where the last equality follows from (20). As the stretched phase does not exhibit extension fluctuations, the only source for fluctuations in z stems from the exchange of contour length between the two phases (fluctuations of ν). We note that the relation

$$\langle \Delta z^2 \rangle = L^2 \langle \Delta\nu^2 \rangle \tag{29}$$

follows directly from the observation that the variance of ν can be obtained from the second derivative of the free energy in g. This is because g and ν enter in the Boltzmann factor of (24) as the combination $g\nu$.

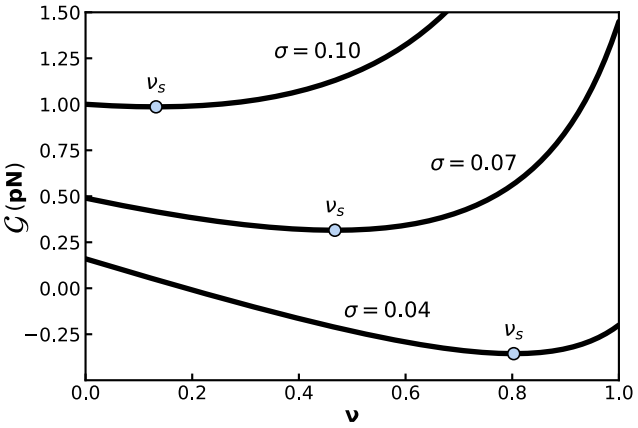

FIG. 2. Plot of $\mathcal{G}(\nu)$, the free energy per unit length (25), vs ν, the fraction of length in the stretched phase. As σ increases, the minimum $\nu_s = \langle \nu \rangle$ shifts towards $\nu = 0$, the pure plectonemic phase. Fluctuations $\langle \Delta\nu^2 \rangle$ are determined by the curvature around the minimum $\mathcal{G}''(\nu_s)$, as given in Eq. (20). The curvature decreases with increasing σ, implying an increase of fluctuations with σ. These curves correspond to $g = 1$ pN, $a = 500$ pN, and $b = 100$ pN ($\mathcal{G}$ is a free energy per unit of length, which means that it has the dimension of a force and is therefore expressed in units of piconewtons).

2. Twistable wormlike chain

To account for the effect of bending fluctuations, we invoke the twistable wormlike chain (TWLC) [19,43–45]. In this model, DNA is represented as an inextensible continuous twistable rod with an associated bending stiffness A and twist stiffness C. The behavior of the TWLC within the extended phase has been studied for both small [46,47] and large forces [40–42]. Here, we use the high-force expansion

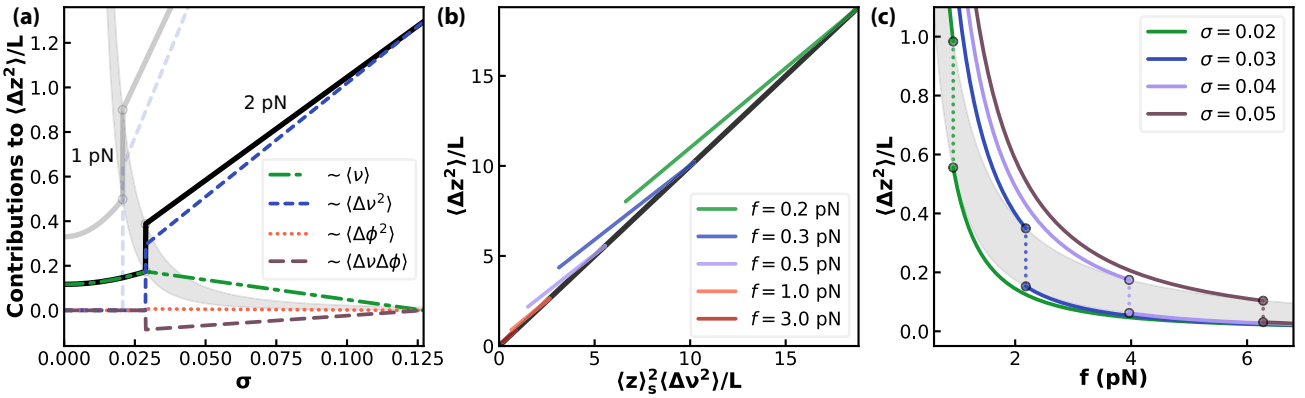

FIG. 3. (a) Plot of the relative extension variance $\langle \Delta z^2 \rangle / L$ vs σ (solid line) and the four different contributions in the postbuckling regime (dashed, dotted, and dash-dotted colored lines) according to the right-hand side of Eq. (32) with the force set to $f = 2$ pN. The plot shows that the leading contribution to $\langle \Delta z^2 \rangle$ is due to length-exchange fluctuations, i.e., the term proportional to $\langle \Delta \nu^2 \rangle$. The variance $\langle \Delta z^2 \rangle$ corresponding to 1 pN is shown in light gray. Jumps in $\langle \Delta z^2 \rangle$ at the buckling transition are indicated by the gray shaded region for a broad range of forces. (b) Master plot showing the dominant contribution of the term proportional to $\langle \Delta \nu^2 \rangle$ to $\langle \Delta z^2 \rangle$. The colored lines are plots of $\langle \Delta z^2 \rangle / L$ vs $\langle z \rangle_S^2 \langle \Delta \nu^2 \rangle / L$ highlighting the agrement with Eq. (36) for different forces and $\sigma_s \leqslant \sigma \leqslant \sigma_p$. The black line is the diagonal $x = y$, indicating perfect agreement between the two quantities. (c) Force dependence of the extension variance $\langle \Delta z^2 \rangle$ for various σ. $\langle \Delta z^2 \rangle$ decreases with increasing f and exhibits a discontinuity at the buckling transition. In this representation the prebuckling regime is located to the right of the buckling point as increasing f favors the extended state over the plectonemic state. Once again the jumps at the buckling transition are indicated by the gray shaded region—this time for a range of σ. For the calculations reported in these plots we used $A = 40$ nm, $C = 100$ nm, $P = 20$ nm, and $\omega_0 = 1.76$ nm^{-1} (corresponding to one full turn of the helix each 10.5 bp).

of the stretched phase free energy, which is given by Eq. (16) with

$$g(f) = f\left(1 - \sqrt{\frac{k_B T}{A f}} + \cdots\right), \tag{30}$$

$$a(f) = \frac{C}{2}\left(1 - \frac{C}{4A}\sqrt{\frac{k_B T}{A f}} + \cdots\right) k_B T \omega_0^2, \tag{31}$$

where $\omega_0 \approx 1.76$ nm^{-1} is the intrinsic helical twist of DNA. Note that in the limit $A \to \infty$, which amounts to suppressing bending fluctuations, one recovers the rigid rod model of Sec. II B 1.

Without making any particular choice for the plectoneme free energy $\mathcal{P}$, the extension variance z can be expressed in terms of the fluctuations of ν and ϕ. Double differentiation of the postbuckling free energy (19) in f [see Eq. (8)] leads to the relation (details are given in Appendix B)

$$\begin{aligned}\langle \Delta z^2 \rangle = {} & k_B T L \langle \nu \rangle \left(g_{ff} - a_{ff}\sigma_s^2\right) \\ & + L^2\left[\left(g_f - a_f \sigma_s^2\right)^2 \langle \Delta \nu^2 \rangle + 4 a_f^2 \langle \nu \rangle^2 \sigma_s^2 \langle \Delta \phi^2 \rangle \right. \\ & \left. - 4 a_f \langle \nu \rangle \sigma_s \left(g_f - a_f \sigma_s^2\right) \langle \Delta \nu \Delta \phi \rangle\right],\end{aligned} \tag{32}$$

where we omitted higher-than-second-order cumulants and adopted the shorthand notation $g_f \equiv dg/df$, $g_{ff} \equiv d^2 g/df^2$, $a_f \equiv da/df$, and $a_{ff} \equiv d^2 a/df^2$. The correlators $\langle \Delta \nu^2 \rangle$, $\langle \Delta \phi^2 \rangle$, and $\langle \Delta \nu \Delta \phi \rangle$ scale as $1/L$ [see Eqs. (20)–(22)], while $\langle \nu \rangle$ is independent of L, such that all the terms on the right-hand side of (32) scale as L, i.e., they retain their relevance for large L. Note that (32) reduces to (29) in the rigid rod limit $g_f = 1$ and $a_f = a_{ff} = g_{ff} = 0$.

Equation (32) decomposes $\langle \Delta z^2 \rangle$ into contributions stemming from different fluctuating quantities. For example, the innate stretched phase variance $\langle \Delta z^2 \rangle$ for a domain of length L_s with supercoiling density σ_s is

$$\langle \Delta z^2 \rangle_{\mathcal{S}} = -k_B T L_s \frac{d^2 \mathcal{S}}{df^2} = k_B T L_s (g_{ff} - a_{ff}\sigma^2). \tag{33}$$

At mean fractional occupancy $\langle \nu \rangle$, this domain length is $L_s = \langle \nu \rangle L$, which yields the first term in Eq. (32).

Evaluation of the remaining contribution requires the calculation of the correlators, which depend on the specific functional form of the plectoneme free energy $\mathcal{P}$. Following prior work [15,48], we invoke the harmonic form (17) with the conventional parametrization [15]

$$b = \tfrac{1}{2} P k_B T \omega_0^2, \tag{34}$$

where P is usually referred to as the effective torsional stiffness of the plectonemic phase [48], which like A and C is expressed in units of length. A plot of $\langle \Delta z^2 \rangle$, as well as the four different contributions on the right-hand side of Eq. (32), as a function of σ for $f = 2.0$ pN is shown in Fig. 3(a). In the prebuckling regime, the stretched phase fully occupies the chain such that $\nu = 1$ and $\phi = \sigma$ remain constant, leaving Eq. (33) with $L_s = L$ as the only nonzero contribution to $\langle \Delta z^2 \rangle$. This contribution decreases linearly in σ in the postbuckling regime, reflecting the decrease of $\langle \nu \rangle$ with σ. Generally, as a consequence of the linear dependence of the free energy (19) on σ in this regime, all four contributions to $\langle \Delta z^2 \rangle$ scale linearly with σ. We note that the term proportional to $\langle \Delta \phi^2 \rangle$ provides a very small contribution to $\langle \Delta z^2 \rangle$. The term proportional to the mixed correlator $\langle \Delta \nu \Delta \phi \rangle$ gives an overall negative contribution to $\langle \Delta z^2 \rangle$, partially canceling the contribution of the stretched phase fluctuations proportional to $\langle \nu \rangle$.

Figure 3(a) highlights that the leading contribution to $\langle \Delta z^2 \rangle$ comes from the term proportional to the phase-exchange fluctuations $\langle \Delta \nu^2 \rangle$. We can rewrite this term by

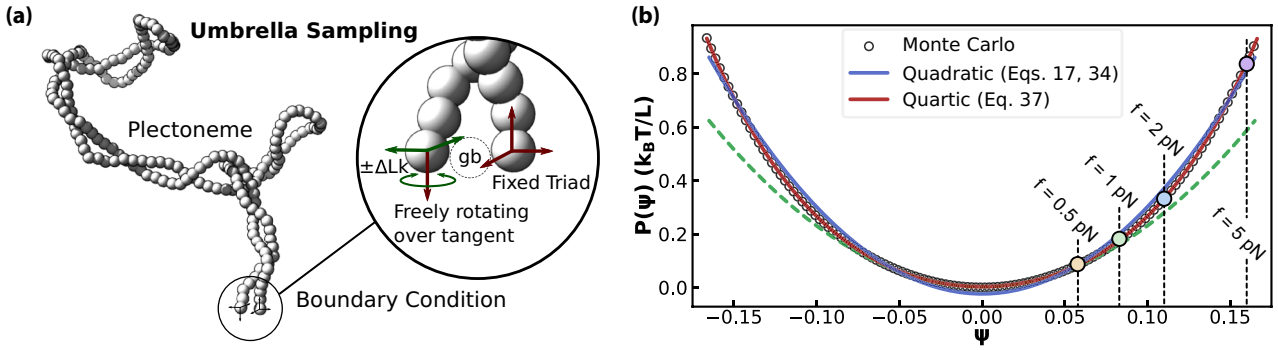

FIG. 4. (a) Snapshot of MC simulation used to calculate the free energy of the plectonemic phase $\mathcal{P}(\psi)$, via umbrella sampling. The first and last beads are maintained fixed in space 8 nm apart, with an antiparallel orientation of their local tangents. The triad attached to the first bead is fully prevented from rotating, and that attached to the last bead is only permitted to rotate freely about its tangent, allowing for diffusion of torsional strain into and out of the system. Between these boundary beads, we place demobilized ghost beads (gb's) to prevent any part of the molecule from crossing through the open gap. By initializing each simulation with zero linking number, the linking number at any snapshot is given by the accumulative rotation angle of the last triad. High supercoiling densities σ are induced by introducing biasing torques. We perform simulations for torques ranging from -36 to 36 pN nm spaced in integer steps to sample the free energy in ψ in the range $-0.19 \leqslant \psi \leqslant 0.19$. (b) Monte Carlo sampled free energy (circles) and approximations with quadratic and quartic models. Best agreement with the quadratic model equation (34) is found for $P = 20.5 \pm 1.7$ nm (solid blue line). Considering the quartic model equation (37) (solid red line) improves the agreement with the MC free energy. The corresponding best fitting parameters are $P_2 = 14.4 \pm 0.3$ nm and $P_4 = (52 \pm 3) \times 10$ nm. A plot of the quadratic free energy with $P = P_2$ is given by the green dashed line. The dashed vertical lines indicate the estimated values of σ_p (the average $\langle\psi\rangle$) for four different forces. The largest source of uncertainty for all reported fitting parameters is found to stem from the chosen range of ψ. In particular, fitting the quadratic parameter P to a higher-order free energy is expected to yield significantly interval dependent results. Similarly, contributions beyond quartic order will lead to a range dependence of P_2 and P_4. Reported uncertainties for these three parameters represent the variability (largest deviation) when varying the upper and lower bound of the ψ from $|\psi| = 0.14$ to $|\psi| = 0.19$. Convergence of the computed free energy is ascertained by applying the WHAM algorithm to ten independent sets of simulations, each consisting of 73×10^6 data points (10^6 per biasing torque) obtained by sampling once every 10^3 Monte Carlo steps. The standard deviation on the three parameters across these ten sets is found to be at least an order or magnitude smaller than the reported uncertainty, such that we consider the free-energy calculation to be sufficiently converged. Our umbrella sampling simulations are similar to those of Ref. [17] performed on a different coarse-grained model of DNA. Deviations from harmonic behavior were already noted yet not quantified in that work.

using the force-extension relation for the stretched phase at supercoiled density σ:

$$\frac{\langle z\rangle_{\mathcal{S}}}{L} = -\frac{d\mathcal{S}}{df} = g_f - a_f\sigma^2. \tag{35}$$

With this, we can then write the leading contribution to the variance of z as

$$\langle \Delta z^2\rangle \approx \langle z\rangle_{\mathcal{S}}^2 \langle \Delta\nu^2\rangle, \tag{36}$$

where $\langle z\rangle_{\mathcal{S}}$ is computed at σ_s. Figure 3(b) shows a plot of $\langle \Delta z^2\rangle$ vs $\langle z\rangle_{\mathcal{S}}^2 \langle \Delta\nu^2\rangle$ for different forces and $\sigma_s \leqslant \sigma \leqslant \sigma_p$ indicating good agreement between the two terms. The force dependence of $\langle \Delta z^2\rangle$ for a selection of supercoiling densities σ is shown in Fig. 3(c). For all σ there is a characteristic force for which $\langle \Delta z^2\rangle$ shows a discontinuous drop, which corresponds to the transition from the postbuckling regime to the prebuckling regime.

III. TWISTABLE WORMLIKE CHAIN MONTE CARLO

We tested the predictions of the two-phase model by means of Monte Carlo (MC) simulations of the discrete twistable wormlike chain (TWLC); see, e.g., Ref. [37]. The discrete TWLC consists of a series of spherical beads carrying each an orthonormal triad of unit vectors [Fig. 4(a)]. In our simulations, each coarse-grained bead corresponds to 10 bp of DNA. From the relative orientations between two consecutive triads, we compute bending and twist angles. The TWLC bending and twist energy is calculated from the bending and torsional stiffnesses given by the two parameters A and C, respectively. Following Rybenkov *et al.* [49], we account for both salt-concentration-dependent electrostatic repulsion and steric hindrance by hard spheres with an effective diameter d_{EV} that exceeds the physical extension of the underlying molecule. Throughout this paper we use $d_{\mathrm{EV}} = 4.0$ nm, $A = 40$ nm, and $C = 100$ nm, which were shown to produce the best agreement with magnetic tweezers measurements in a buffer of 150 mM univalent salt [37]. Further details on the simulation protocol are provided in Appendix C.

A. Plectoneme free energy

In a first step, we utilize the MC simulations to explore the free energy of the plectonemic phase $\mathcal{P}(\psi)$ by umbrella sampling [50]. With appropriately imposed boundary conditions, we restrict simulations of chains of length $L = 680$ nm (2 kbp) to the plectonemic phase [see Fig. 4(a) and caption for details] and repeat the simulation for a range of biasing torques to sample supercoiling densities ψ in the range of $-0.165 \leqslant \psi \leqslant 0.165$. A single unbiased histogram combining all individual biased histograms in ψ is constructed by employing the weighted histogram analysis method (WHAM) [51]. Boltzmann inversion then yields the sought plectoneme free energy $\mathcal{P}(\psi)$; see Fig. 4(b). The best fit for the effective

torsional stiffness of the plectonemic state for the quadratic model $\mathcal{P} = b\psi^2$ [with the parametrization of Eq. (34)] over the entire sampled range is found to be $P = 20.5 \pm 1.7$ nm (for details on the calculation of the uncertainty, see caption of Fig. 4), which is consistent with previous experimental measurements [37,48]. However, closer inspection shows that MC data deviate from the quadratic model free energy. Instead, the quartic functional form

$$\mathcal{P}(\psi) = \left(\frac{P_2}{2}\psi^2 + \frac{P_4}{4}\psi^4\right)\omega_0^2 k_B T, \tag{37}$$

is found to agree significantly better with the sampled energy. As the supercoiling density ψ is dimensionless, both P_4 and P_2 have the unit of a length. Smallest least-squares differences are attained for the coefficients $P_2 = 14.4 \pm 0.3$ nm and $P_4 = (52 \pm 3) \times 10$ nm. For $\psi < 0.075$ the relative contribution of the quartic term is less than 10% (and less than 5% for $\psi < 0.05$), suggesting the quadratic model to be a reasonable approximation in this regime, albeit with a stiffness of P_2, which is about 25% lower than the consensus values reported in the literature [37,48]. We note that deviations from the quadratic behavior become more relevant at high tension as the average supercoil density of the plectonemic phase $\sigma_p = \langle\psi\rangle$ becomes larger in this regime [σ_s and σ_p grow with f; see Eqs. (18) and recall that $g \sim f$]. Therefore it becomes increasingly important to include the quartic terms as the tension increases. Values of σ_p for four different forces within the range of forces typically considered in MT experiments, representing the supercoiling density in the respective plectonemic domains, are indicated as vertical dashed lines in Fig. 4(b).

It is important to note that the double-tangent construction [Eq. (5)] is determined not only by the free energies $\mathcal{S}(\phi, f)$ and $\mathcal{P}(\psi)$, but also by their local derivatives. While the global quadratic fit of the free energy may appear to be a reasonable approximation for $\mathcal{P}$ over the full range of ψ, the quartic term is necessary for a good approximation of the free-energy derivatives $\mathcal{P}_\psi$ and $\mathcal{P}_{\psi\psi}$ [the latter contributes to the variances (10) and (13)].

B. The mean extension and the extension variance

Next, we consider linear DNA molecules of length $L = 2692.8$ nm (7920 bp), subject to different stretching forces (0.5–5 pN). We performed Monte Carlo simulations in the fixed linking number ensemble within a range of relevant supercoiling densities. From the sampled ensembles, we obtain data of mean extension $\langle z\rangle$ [Fig. 5(a)] and extension variance $\langle\Delta z^2\rangle$ [Fig. 5(b)], which we compare with the predictions of the two-phase model. For the stretched phase free energy, we use Eq. (16) with $g(f)$ and $a(f)$ defined by Eqs. (30) and (31). We include the next-higher-order term in the expansion of g:

$$g(f) = f\left(1 - \sqrt{\frac{k_B T}{Af}} + g_2\frac{k_B T}{Af}\right). \tag{38}$$

Using the numerically exact solution of a stretched wormlike chain [41], we find $g_2 = 0.3$ for $A = 40$ nm, and the room temperature value $k_B T = 4.1$ pN nm. The term proportional to g_2 contributes as an overall force-independent constant to the stretched phase free energy and thus does not modify the statistical properties of this phase. However, g_2 is relevant in the double-tangent construction as it gives a constant relative shift to the stretched and plectoneme phase free energies.

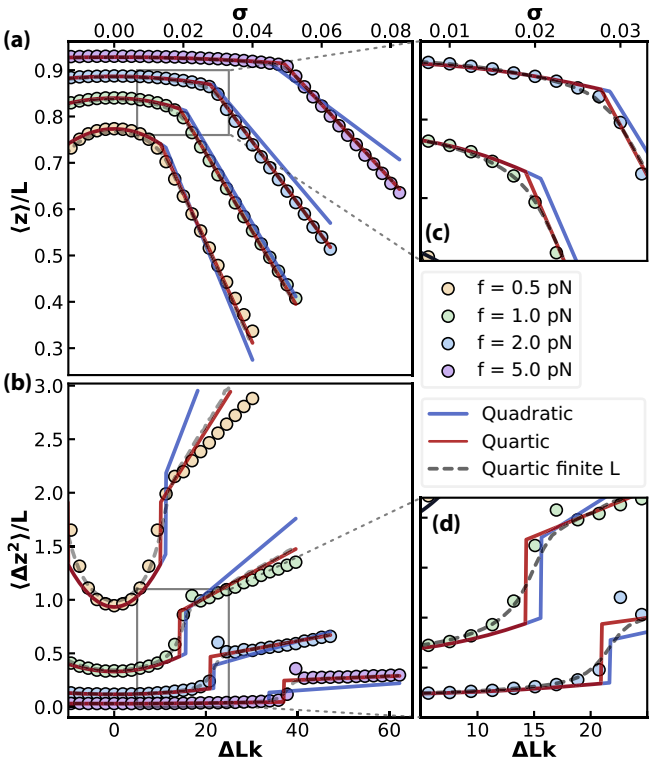

FIG. 5. Rotation curves of (a) extension and (b) extension variance as a function of applied turns (ΔLk or σ) for four different stretching forces (0.5, 1, 2, and 5 pN). Colored markers show $\langle z\rangle$ and $\langle\Delta z^2\rangle$ for Monte Carlo simulations of the TWLC for a molecule of length $L = 2692.8$ nm (7920 bp). For each combination of force and linking density we performed 10^{11} Monte Carlo steps, sampling the extension every 100 steps. Solid blue lines give the respective values for the two-phase model with quadratic plectoneme free energy $\mathcal{P}$ using $P = 20.5$ nm. Two-phase model curves with quartic $\mathcal{P}$ using $P_2 = 14.4$ nm and $P_4 = 524$ nm are shown as solid red lines. Thick gray dashed lines show the numerical integration of the two-phase model with quartic free energy. (c) and (d) show a zoom-in on the buckling transition for $\langle z\rangle$ and $\langle\Delta z^2\rangle$, respectively. The finite-length numerical calculation, with L matching the chain length considered in the Monte Carlo simulations, is indicated by the gray dashed line.

The quadratic free-energy two-phase model as defined in Eq. (34) using the umbrella sampled full-range optimization $P = 20.5$ nm yields reasonable agreement with the MC sampled mean extension $\langle z\rangle$, albeit with visible deviations in the postbuckling slopes. As anticipated in the discussion of the free energy, the most substantial deviations are observed for large forces. Large forces imply tight plectonemic coiling (large $\langle\psi\rangle = \sigma_p$), where the deviation of $\mathcal{P}$ from the quadratic model is most notable; see Fig. 4(a). The deviations between theory and simulations are almost entirely resolved by invoking the quartic model (37), which yields excellent agreement with the mean extension of the MC data across the full range of forces.

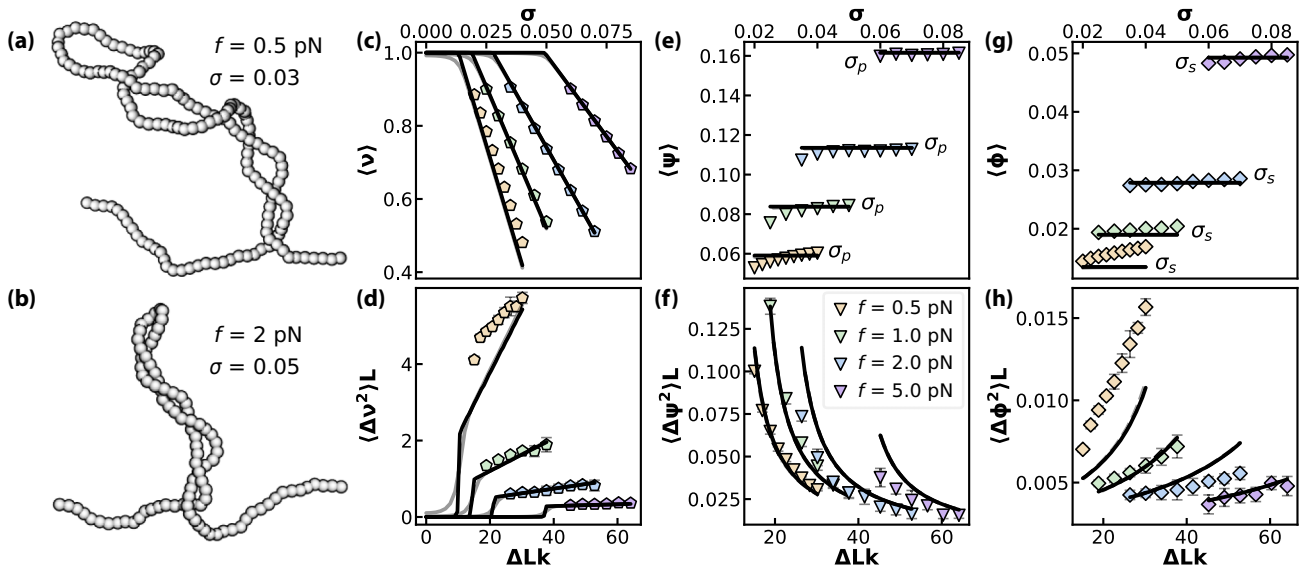

FIG. 6. (a) and (b) Snapshots of MC simulations for two different forces. At higher tension (b) the plectoneme is considerably tighter than at lower tension (a), which is reflected by a significantly larger supercoiling density σ_p. (c)–(h) Using our plectoneme-detecting algorithm (Appendix D), we have computed averages and variances of the fraction of length in the straight phase ν [(c) and (d)] and the supercoiling density of the plectonemic phase ψ [(e) and (f)] and of the straight phase ϕ [(g) and (h)]. Solid lines in (c)–(h) are the predictions of the two-phase model, using the quartic free energy for the plectonemic phase (37) and the expansion (38) for $g(f)$.

In spite of the success of the quartic model for the mean extension, the variance reveals the existence of remnant shortcomings. While general features are quite accurately reproduced and the high-force agreement is rather convincing, the slope of the low-force variance significantly overestimates the MC data. Nonetheless, the quartic free energy constitutes a compelling improvement to the quadratic model.

We also performed a numerical integration of the full partition function. This reveals finite-L effects that are not captured by the free-energy minimization approach (3), which is valid in the thermodynamic limit. The difference between the two calculations is most visible in the vicinity of the phase boundary $\sigma = \sigma_s$ [see Figs. 5(c) and 5(d)]. Here, the Gaussian approximation predicts a jump of $\langle \Delta z^2 \rangle$, while the numerical integration smoothly connects the pre- and postbuckling regimes and matches the simulation data in the prebuckling regime.

C. Two-phase model degrees of freedom

Inspired by previous work [18,52,53], we developed an algorithm to detect the regions occupied by the plectonemic phase in simulation generated snapshots (see Appendix D for details). With this algorithm we calculated the total fraction of stretched phase ν and the supercoiling densities of the stretched and plectonemic phases, ϕ and ψ. A comparison of these results with the prediction of the two-phase model, employing the quartic model [Eq. (37)] for the plectoneme free energy with the parameters obtained from umbrella sampling, is shown in Fig. 6. The averages $\langle \nu \rangle$, $\langle \psi \rangle$, and $\langle \phi \rangle$ convincingly follow the prediction of the two-phase model, at least for large forces [Figs. 6(c), 6(e), and 6(g)]. We note that $\langle \nu \rangle$ is linear in σ, as expected from Eq. (6). Moreover, $\langle \phi \rangle = \sigma_s$ and $\langle \psi \rangle = \sigma_p$ are approximately independent of σ. Deviations are apparent for the smallest force (0.5 pN) and close to the buckling point $\sigma \approx \sigma_p$, where finite-length effects are of relevance. The variances $\langle \Delta \nu^2 \rangle$, $\langle \Delta \psi^2 \rangle$, and $\langle \Delta \phi^2 \rangle$ show stronger deviations from the theory as compared with the averages, especially at the smallest analyzed force ($f = 0.5$ pN). Considering the inherent difficulty in determining phase boundaries, and the sensitivity of higher moments to algorithmic noise, we observe satisfactory agreement between theory and simulations for the variances of ν, ψ, and ϕ [Figs. 6(d), 6(f), and 6(h)]. For all forces, the two-phase model theory qualitatively captures the general trends of the fluctuations. Quantitative agreement is once again limited to the higher-force regime $f \gtrsim 1$ pN.

D. Contributions to extension variance

Finally, we verify whether the conclusions of Sec. II B 2 that were obtained for the two-phase model with quadratic free energies still hold for a quartic plectoneme free energy and for the TWLC Monte Carlo simulations. The expectation values for $\langle \nu \rangle$, $\langle \Delta \nu^2 \rangle$, $\langle \Delta \phi^2 \rangle$, and $\langle \Delta \nu \Delta \phi \rangle$, calculated numerically for quartic $\mathcal{P}$ and deduced from TWLC Monte Carlo simulations as shown in Fig. 6, allow us to once again decompose the extension variance into various contributions according to Eq. (32). Note that this equation remains valid as long as the stretched phase free energy is reasonably well approximated by the stretching free energy (30) and twist free energy (31). Given the excellent agreement between the theoretical and simulated $\langle z \rangle$ and $\langle \Delta z^2 \rangle$ in the prebuckling regime (see Fig. 5), we consider this requirement satisfied. The differences between the quadratic and quartic $\mathcal{P}$ are fully contained in the the correlators [see Eq. (32)] which were deduced from the simulations in the previous section.

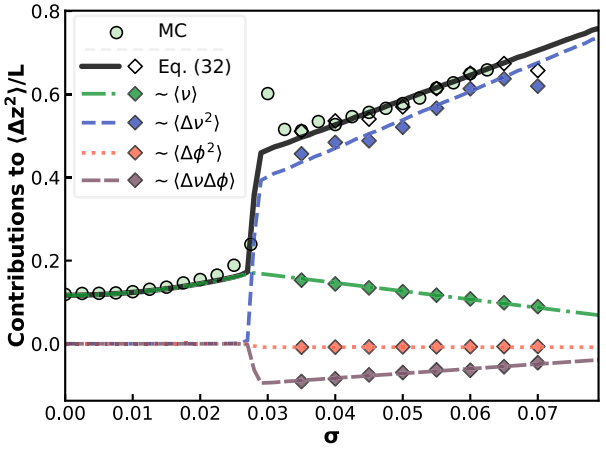

FIG. 7. Comparison of the extension variance $\langle \Delta z^2 \rangle$ for $f = 2$ pN (black solid line, theory with quartic $\mathcal{P}$; round symbols, TWLC MC) with the four different contributions according to Eq. (32) (blue, term $\sim \langle \Delta \nu^2 \rangle$; green, term $\sim \langle \nu \rangle$; orange, term $\sim \langle \Delta \phi^2 \rangle$; brown, term $\sim \langle \Delta \nu \Delta \phi \rangle$). The numerical calculations with quartic $\mathcal{P}$ are shown as lines, and those with MC data are shown as diamonds. White diamonds represent the sum of the MC extracted contributions.

In Fig. 7 the extension variance of the TWLC Monte Carlo simulations for $f = 2$ pN is compared with the contributions stemming from $\langle \nu \rangle$, $\langle \Delta \nu^2 \rangle$, $\langle \Delta \phi^2 \rangle$, and $\langle \Delta \nu \Delta \phi \rangle$ according to Eq. (32). Just as in the case of the quadratic free energy, the extension variance $\langle \Delta z^2 \rangle$ is dominated by phase-exchange fluctuations $\langle \Delta \nu^2 \rangle$, especially for large supercoiling densities, where the system shows a significant occupancy of the plectonemic phase.

IV. CONCLUSION

In this paper, we discussed the properties of end-point fluctuations of linear stretched and overtwisted DNA. This is the typical setup of single-molecule MT experiments, in which a magnetic field is used to apply a stretching force f and to maintain kbp-long DNA molecules at a fixed linking number. We based our analysis on a two-phase model [15], which describes DNA buckling as a thermodynamic first-order transition.

In the prebuckling regime, both mean extension $\langle z \rangle$ and extension fluctuations, characterized by the variance $\langle \Delta z^2 \rangle$, are controlled by the behavior of the stretched phase. Past the buckling point, the DNA consists of coexisting stretched and plectonemic domains. The average length of the plectonemic phase increases with increasing supercoiling density σ, while the stretched phase decreases, leading to a global decrease of $\langle z \rangle$. The two-phase model indicates that several terms contribute to $\langle \Delta z^2 \rangle$, representing distinct fluctuation mechanisms; see Eq. (32). While $\langle \Delta z^2 \rangle$ linearly increases with σ at postbuckling, the contribution of extension fluctuations of the stretched phase [term proportional to ν in (32)] decreases, as this phase decreases in length. We show that among all the contributions to $\langle \Delta z^2 \rangle$, phase-exchange fluctuations, e.g., the transient exchange of lengths between the stretched and the plectonemic phases through which the plectonemes shrink and grow, are the dominant one. Equation (36), which approximates (32), summarizes the dominance of the length-exchange mechanism. The remaining contributions to the extension variance $\langle \Delta z^2 \rangle$ are due to fluctuations of the supercoiling densities of the stretched and plectonemic phases and of mixed terms coupling the stretched phase length and supercoiling density. Although the overall contribution of these terms to $\langle \Delta z^2 \rangle$ is minor, we note a perhaps curious cancellation between a (positive) stretched phase fluctuation term and a (negative) mixed correlator term. These two contributions are indicated as $\sim \langle \nu \rangle$ and $\sim \langle \Delta \phi \Delta \nu \rangle$ in Figs. 3(a) and 7. The contribution to $\langle \Delta z^2 \rangle$ due to the fluctuations of stretched phase supercoil density [term indicated with $\sim \langle \Delta \phi^2 \rangle$ in Figs. 3(a) and 7] is generally small.

We corroborate these theoretical predictions with Monte Carlo simulations of the discrete TWLC. In a first step, we ascertain the most appropriate form for the plectonemic free energy $\mathcal{P}$ by umbrella sampling. We find that the quadratic free energy (17) is a good approximation only for plectoneme supercoiling densities σ_p smaller than roughly 0.05. Beyond that, the quartic (37) is found to yield satisfactory agreement. For large forces, the use of the quartic $\mathcal{P}$ is found to significantly increase the agreement between theoretical extension and extension variance curves and Monte Carlo sampled data, as compared with the previously used quadratic [15,37]. Our analysis suggests that the two-phase model captures the phenomenology of the fluctuations in the postbuckling regime. Discrepancies observed at small forces ($f \leqslant 1$ pN) are likely due to a breakdown of the two-phase model description. In particular, interfacial regions (plectoneme tails) connecting stretched and plectonemic domains are becoming increasingly extensive at small forces, leading to an inherent difficulty of sharply distinguishing the two domains. In spite of these deviations, the overall qualitative picture holds also at small forces.

The focus of this work is limited to equilibrium properties of fluctuations of stretched and torsionally constrained DNA. Our theory and simulations do not address characteristic time scales associated with these fluctuations. Experiments revealed several mechanisms of supercoiled DNA dynamics with plectonemes performing local diffusive as well as nonlocal jumps [25]. We note that phase-exchange fluctuations do not necessarily induce a displacement of the plectoneme, which could shrink and grow without diffusing as a whole. It is likely that the time scales of phase-exchange fluctuations are shorter than those of plectoneme diffusion, but a more detailed analysis (via molecular dynamics simulations) would be necessary to gain more insights into the dynamics of plectonemes.

Summarizing, we believe that an in-depth understanding of the nature of equilibrium fluctuations of stretched supercoiled DNA is important, since in the cell, as well as in *in vitro* experiments, DNA is subject to strong thermal fluctuations. Moreover, fluctuations can carry information about processes that do not affect average quantities, as was illustrated in a recent study on protein binding in the context of supercoiled DNA [37].

ACKNOWLEDGMENTS

Discussions with Pauline Kolbeck, Jan Lipfert, Midas Segers, and Willem Vanderlinden are gratefully acknowledged. E.S. acknowledges financial support from Fonds Wetenschappelijk Onderzoek-Vlaanderen (FWO) Grant No. 1SB4219N.

APPENDIX A: GAUSSIAN FLUCTUATIONS OF ν AND ϕ

Here, we provide additional details on the calculations of the fluctuations in ν, ϕ, and ψ given in Eqs. (10)–(13). We use the same notation as in the main text: Subscripts denote differentiation with respect to the indicated variable, followed by evaluation at the minimum. For example,

$$\mathcal{P}_\psi = \left.\frac{d\mathcal{P}}{d\psi}\right|_{\psi=\sigma_p}, \quad \psi_\nu = \left.\frac{d\psi}{d\nu}\right|_{\phi=\sigma_s,\nu=\nu_s}. \tag{A1}$$

Using the expression for the free energy (2), we find for the second derivative in ν

$$\begin{aligned}\mathcal{F}_{\nu\nu} &= -2\mathcal{P}_\psi\psi_\nu + (1-\nu_s)\big(\mathcal{P}_\psi\psi_{\nu\nu} + \mathcal{P}_{\psi\psi}\psi_\nu^2\big)\\ &= (1-\nu_s)\mathcal{P}_{\psi\psi}\psi_\nu^2 = \frac{(\sigma_p-\sigma_s)^2}{1-\nu_s}\mathcal{P}_{\psi\psi},\end{aligned} \tag{A2}$$

where we have used the following relations:

$$\psi = \frac{\sigma-\phi}{1-\nu} - \phi, \tag{A3}$$

$$\psi_\nu = \frac{\sigma-\sigma_s}{(1-\nu_s)^2} = \frac{\sigma_p-\sigma_s}{1-\nu_s}, \tag{A4}$$

$$\psi_{\nu\nu} = 2\frac{\sigma-\sigma_s}{(1-\nu_s)^3} = \frac{2\psi_\nu}{1-\nu_s}. \tag{A5}$$

Likewise, we find for the other derivatives

$$\mathcal{F}_{\phi\phi} = \frac{\nu_s}{1-\nu_s}[(1-\nu_s)\mathcal{S}_{\phi\phi} + \nu_s\mathcal{P}_{\psi\psi}], \tag{A6}$$

$$\mathcal{F}_{\phi\nu} = \frac{\nu_s}{1-\nu_s}(\sigma_p-\sigma_s)\mathcal{P}_{\psi\psi}. \tag{A7}$$

Equipartition then stipulates that fluctuations in ϕ and ν are obtained from the inversion of the Hessian matrix. This gives

$$\beta L\langle\Delta\nu^2\rangle = \frac{\mathcal{F}_{\phi\phi}}{\mathcal{F}_{\nu\nu}\mathcal{F}_{\phi\phi}-\mathcal{F}_{\nu\phi}^2}, \tag{A8}$$

$$\beta L\langle\Delta\phi^2\rangle = \frac{\mathcal{F}_{\nu\nu}}{\mathcal{F}_{\nu\nu}\mathcal{F}_{\phi\phi}-\mathcal{F}_{\nu\phi}^2}, \tag{A9}$$

$$\beta L\langle\Delta\nu\Delta\phi\rangle = -\frac{\mathcal{F}_{\nu\phi}}{\mathcal{F}_{\nu\nu}\mathcal{F}_{\phi\phi}-\mathcal{F}_{\nu\phi}^2}. \tag{A10}$$

Replacing (A2), (A6), and (A7) in the previous relations, we get Eqs. (10)–(12), respectively.

APPENDIX B: DERIVATION OF $\langle\Delta z^2\rangle$ FOR THE TWLC

The free energy per unit length of the quadratic model in the postbuckling regime (19) depends on the force f via the variables $a(f)$ and $g(f)$. Differentiation with respect to f can be expressed via the partial derivatives with respect to a and g as

$$\mathcal{F}_f = \mathcal{F}_g g_f + \mathcal{F}_a a_f, \tag{B1}$$

where we use the notation $\Psi_f \equiv d\Psi/df$ for the total derivative in f and $\Psi_a \equiv \partial\Psi/\partial a$ and $\Psi_g \equiv \partial\Psi/\partial g$ for partial derivatives in a and g. The second derivative in f gives the variance of z, which can then be written as

$$\begin{aligned}\beta\frac{\langle\Delta z^2\rangle}{L} &= -\mathcal{F}_{ff} = -\big(\mathcal{F}_g g_{ff} + \mathcal{F}_a a_{ff} + \mathcal{F}_{gg} g_f^2\\ &\quad + \mathcal{F}_{aa} a_f^2 + 2\mathcal{F}_{ag} a_f g_f\big)\\ &= \langle\nu\rangle g_{ff} - \langle\nu\phi^2\rangle a_{ff} + \beta L\big[\langle\Delta\nu^2\rangle g_f^2\\ &\quad + \langle\Delta(\nu\phi^2)^2\rangle a_f^2 - 2(\langle\nu^2\phi^2\rangle - \langle\nu\rangle\langle\nu\phi^2\rangle)a_f g_f\big],\end{aligned} \tag{B2}$$

where we have expressed derivatives with respect to a and g as correlators of combinations of variables ν and ϕ using

$$\mathcal{F}_g = -\langle\nu\rangle, \quad \mathcal{F}_{gg} = -\beta L\langle\Delta\nu^2\rangle, \tag{B3}$$

$$\mathcal{F}_a = \langle\nu\phi^2\rangle, \quad \mathcal{F}_{aa} = -\beta L\langle\Delta(\nu\phi^2)^2\rangle, \tag{B4}$$

$$\mathcal{F}_{ag} = \beta L(\langle\nu^2\phi^2\rangle - \langle\nu\rangle\langle\nu\phi^2\rangle), \tag{B5}$$

which can be obtained from the form of the free energy. These correlators can be further expanded to lowest order in fluctuations around the averages $\Delta\phi = \phi - \sigma_s$ and $\Delta\nu = \nu - \nu_s$ (recall that $\nu_s = \langle\nu\rangle$ and $\sigma_s = \langle\phi\rangle$).

For example, for the term $\langle\nu\phi^2\rangle$, this expansion gives

$$\langle\nu\phi^2\rangle \approx \nu_s\sigma_s^2 + \nu_s\langle\Delta\phi^2\rangle + 2\sigma_s\langle\Delta\nu\Delta\phi\rangle. \tag{B6}$$

Similar relations can be obtained for $\langle\nu^2\phi^2\rangle$ and $\langle\Delta(\nu\phi^2)^2\rangle$. Substituting these in (B2), we can express the variance in z as a function of the correlators $\langle\Delta\nu^2\rangle$, $\langle\Delta\phi^2\rangle$, and $\langle\Delta\nu\Delta\phi\rangle$, which gives Eq. (32).

APPENDIX C: MONTE CARLO SIMULATIONS

In this Appendix, additional information about the employed Monte Carlo simulations is provided.

1. DNA representation

The Monte Carlo simulations were performed using the triad model representation of DNA as utilized in prior works [37,44,54,55]. Segments of 10 bp are coarse grained into a single rigid body, captured by a position vector and local material frame (triad) $\widehat{\mathcal{T}} = \{\widehat{\mathbf{e}}_1, \widehat{\mathbf{e}}_2, \widehat{\mathbf{e}}_3\}$, which encapsulates both the direction of the local tangent as well as the information necessary to trace torsional strains. Rotations connecting successive triads are parametrized as Euler vectors (rotation vectors) $\mathbf{\Omega}$ pointing in the direction of the respective rotational axes with magnitudes equal to the rotation angles. Projection of a given such vector onto the three axes of either of the two associated triads $\Omega_i \equiv \mathbf{\Omega}\cdot\widehat{\mathbf{e}}_i$ yields three separate rotational components, which are identified as bending (Ω_1 and Ω_2) and twist (Ω_3) components. With this parametrization, molecules of length $L = Na$, i.e., consisting of N coarse-grained segments of length $a = 3.4$ nm, may be represented by the discretized TWLC free energy

$$\beta E_{\mathrm{TWLC}} = \frac{1}{2a}\sum_{n=1}^{N}\big[A\big(\Omega_1^2 + \Omega_2^2\big) + C\Omega_3^2\big], \tag{C1}$$

where A and C are the bending and twist stiffnesses, respectively. Stretching forces are included in the energy functional as fields conjugate to the end-to-end vector $\mathbf{R}$:

$$E_f = -\mathbf{f} \cdot \mathbf{R}. \tag{C2}$$

Furthermore, steric hindrance and screened electrostatic repulsion between the negatively charged DNA backbones are conjointly realized by hard sphere potentials [49] with a diameter of $d_{\mathrm{EV}} = 4.0$ nm, which was found to yield good agreement with magnetic tweezer data conducted in a buffer of 150 mM univalent salt [37].

2. Sampling procedure

Ensembles of equilibrium configurations for the described model are generated by initializing fully elongated configurations of chain segments followed by iterative generation of new configurations. Acceptance or rejection of trial configurations is based on the Metropolis criterion.

For the extended DNA simulations, aimed at mimicking the setup of magnetic tweezer measurements, trial configurations are constructed by a combination of crankshaft and pivot moves [18,52,56–58]. Since these simulations are meant to generate a fixed linking number ensemble, care has to be taken to identify and reject linking-number-changing moves. This is achieved by the combination of three separate mechanisms. Firstly, impenetrable planes normal to the force director field are attached to the two termini, such that all chain segments remain strictly between these planes. Allowing the chain to pass behind those termini can lead to a change of linking number. Secondly, all configurational permutations are evaluated as collective continuous transformations of the positions of the involved segments. Overlap of the spherical excluded volume attached to any pair of segments at any point along the traced paths, save for neighboring segments, which may overlap by default if $d_{\mathrm{EV}} > a$, immediately prompts the rejection of the proposed configuration. In a prior study the problem of detecting transient overlap during continuous transformations of chain beads was shown to be equivalent to finding the point of closest approach between two line segments [52]. This allows for the efficient evaluation of said condition. Note that the just described acceptance condition automatically covers compliance with the excluded volume interaction. Lastly, the possibility for linking number violation posed by the periodicity of twist angles between successive triads (a change of twist angle $\Delta\Omega_3$ is equivalent to $\Delta\Omega_3 + 2n\pi$ with $n \in \mathbb{Z}$) is eliminated by limiting local twist angles to values smaller than π radians as well as restricting the maximum change in twist angle to $\pi/2$. Changes in local twist that would otherwise lead to dissipation of linking number can thereby always be identified.

The trial configuration procedure employed in the umbrella sampling simulations for the plectoneme free energy is largely identical to the one mentioned before, with the exception that pivot moves are substituted by linking-number-changing moves. For these moves a random segment and random rotation angle $\Delta\theta$ are chosen. All segment triads with index larger than the chosen segment are rotated over their respective tangents by the given angle. This move does not change the position of any of the segments, such that the writhe (Wr) of the configuration remains unaltered. However, the rotation of the last triad by the angle $\Delta\theta$ leads to a change in total twist (Tw) by the same amount. The Călugăreanu-White-Fuller theorem [1–3] (Lk = Tw + Wr) then implies that $\Delta\theta$ equals the change in linking number.

APPENDIX D: DETECTING PLECTONEMES

Here, we outline the algorithm used to detect plectonemic regions in simulation generated configurations. Two different characteristics have been used in the past to identify plectonemes. For one, plectonemic coiling induces a juxtaposition between sites that are far away along the DNA contour. Therefore various studies utilized a distance map (or contact map) to identify regions of high segment proximity [30,53,59]. Alternatively, one can identify plectonemes as regions of high writhe density [18,52]. Writhe (defined below) is a measure of the amount of coiling of a closed curve [1], and plectonemes are characterized by a considerably larger writhe density as compared with the stretched phase (see Fig. 6 and Refs. [52,60]).

In this paper, we used the latter property to identify plectonemes. Since our simulations are composed of a series of $N-1$ straight segments $\mathbf{s}_i$ connecting consecutive beads, the double-integral definition of writhe [1] may be decomposed into $(N-1)^2$ pairwise contributions [61]

$$\mathrm{Wr} = \frac{1}{4\pi} \sum_{i=1}^{N} \sum_{j=1}^{N} \int_{\mathbf{s}_i} \int_{\mathbf{s}_j} \frac{(d\mathbf{r}_j \times d\mathbf{r}_i) \cdot \mathbf{r}_{ij}}{r_{ij}^3} = \sum_{i=1}^{N} \sum_{j=1}^{N} w_{ij}. \tag{D1}$$

The elements w_{ij} may then be viewed as analogous to the entries of a contact map. In practice, we calculate those elements w_{ij} by analytically carrying out the double integral over the two straight segments $\mathbf{s}_i$ and $\mathbf{s}_j$ of length a (3.4 nm in our case). For details on this calculation, see method $1b$ from Ref. [62]. Note, that in the writhe map, plectonemes have much more contrast as compared with the proximity map [52]. An example of a writhe map for a Monte Carlo generated configuration of length $L = 1360$ nm (4000 bp or 400 segments) containing three plectonemes is shown in Fig. 8. The high-contrast black bands trace segment pairs (s_i, s_j), where the ith and jth segments are on opposing strands along the superhelix. Towards the diagonal, as i comes close to j, the trace approaches the plectoneme end loop. Conversely, the outermost segments, indicated by the upper left and lower right corners of the rectangles drawn around the plectonemic region, mark the entry points of the plectonemes.

We trace plectonemes by setting a force-dependent cutoff writhe density χ_{min}, which is typically chosen so as to be somewhere in between the expected stretched and plectonemic phase supercoiling densities σ_s and σ_p. Such a choice can be made more quantitative by also considering the twist density in the chain, which can either be directly calculated from the given snapshots or be calculated from the stretched phase theory [39,42,63],

$$\sigma_{\mathrm{Tw}} = \left(1 - \frac{C}{4A}\sqrt{\frac{k_B T}{Af}}\right)\sigma, \tag{D2}$$

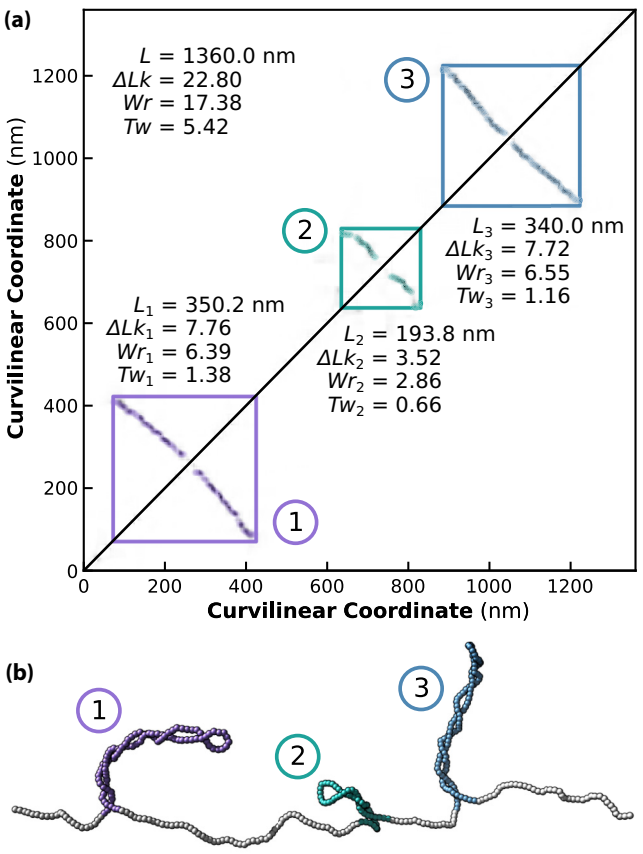

FIG. 8. Illustration of the algorithm used to identify plectonemes in Monte Carlo generated snapshots. (a) Writhe map corresponding to the configuration shown in (b). The three plectonemes of (b) are highlighted by rectangles with corners (i, i), (i, j), (j, i), and (j, j) for a plectoneme with entry and exit indices i and j, respectively. In the figure, these indices have been converted into curvilinear coordinates. Writhe and twist can be calculated separately for each plectoneme, which allows for the calculation of the plectoneme linking number.

as twist is equilibrated over both phases. We then identify all indices i for which the total involved writhe density is at least $\chi_{\min}$, i.e.,

$$W_i \equiv \sum_{j=1}^{N-1} w_{i,j} \geqslant \frac{a\omega_0}{2\pi}\chi_{\min}. \tag{D3}$$

Neighbors among these remaining segments, say, at indices k and l, are then connected, if the sum of the intermediate contributions of W_i, including those at k and l, still exceeds the minimum writhe density, i.e., if

$$\frac{1}{l-k+1}\sum_{j=k}^{l} W_j \geqslant \frac{a\omega_0}{2\pi}\chi_{\min}. \tag{D4}$$

This generates connected regions tracing one strand along a superhelical branch. The branch itself can be traced by identifying for every i the index j for which the writhe contribution $|w_{ij}|$ is largest. Full plectoneme branches are finally identified by finding the pairs of strands which map into each other by reverting the respective indices, which is equivalent to transposing the points relative to the writhe map. Certain care has to be taken when tracing the branches, so as not to pick up contributions stemming from outside the current branch, which could in some cases lead to an erroneous assignment of a part of a stretched domain to a plectoneme. An exhaustive discussion of the algorithm is beyond the scope of this work. The final traces found for each plectoneme are indicated as colored lines in Fig. 8.

Once the plectonemic domains are identified, the contained writhe can be extracted from the writhe map. The twist can either be taken directly from the simulation, if local twist strains are considered, or in the case of equilibrated twist simulations [17,27,57] from the total twist $\mathrm{Tw} = \Delta\mathrm{Lk} - \mathrm{Wr}$ of the snapshot. The summation of writhe and twist contained in the plectonemic domains yields the total linking number in the plectonemic phase, which together with the number of segments in these domains yields the supercoiling density ψ. The calculation of the stretched phase supercoiling density ϕ is completely analogous. Finally, the fraction of segments not contained in plectonemic domains gives the fractional occupancy of the stretched phase ν.

[1] F. B. Fuller, The writhing number of a space curve, Proc. Natl. Acad. Sci. USA **68**, 815 (1971).
[2] J. H. White, Self-linking and the Gauss integral in higher dimensions, Am. J. Math. **91**, 693 (1969).
[3] G. Călugăreanu, Sur les classes d'isotopie des noeuds tridimensionnels et leurs invariants, Czech. Math. J. **11**, 588 (1961).
[4] L. Postow, C. D. Hardy, J. Arsuaga, and N. R. Cozzarelli, Topological domain structure of the *Escherichia coli* chromosome, Genes Dev. **18**, 1766 (2004).
[5] N. Naumova, M. Imakaev, G. Fudenberg, Y. Zhan, B. R. Lajoie, L. A. Mirny, and J. Dekker, Organization of the mitotic chromosome, Science **342**, 948 (2013).
[6] S. Corless and N. Gilbert, Effects of DNA supercoiling on chromatin architecture, Biophys. Rev. **8**, 245 (2016).
[7] W. Vanderlinden, T. Brouns, P. U. Walker, P. J. Kolbeck, L. F. Milles, W. Ott, P. C. Nickels, Z. Debyser, and J. Lipfert, The free energy landscape of retroviral integration, Nat. Commun. **10**, 4738 (2019).
[8] Y. Yan, Y. Ding, F. Leng, D. Dunlap, and L. Finzi, Protein-mediated loops in supercoiled DNA create large topological domains, Nucleic Acids Res. **46**, 4417 (2018).
[9] Y. Yan, F. Leng, L. Finzi, and D. Dunlap, Protein-mediated looping of DNA under tension requires supercoiling, Nucleic Acids Res. **46**, 2370 (2018).
[10] Y. Yan, W. Xu, S. Kumar, A. Zhang, F. Leng, D. Dunlap, and L. Finzi, Negative DNA supercoiling makes protein-mediated looping deterministic and ergodic within the bacterial doubling time, Nucleic Acids Res. **49**, 11550 (2021).
[11] C. J. Dorman and M. J. Dorman, DNA supercoiling is a fundamental regulatory principle in the control of bacterial gene expression, Biophys. Rev. **8**, 89 (2016).

[12] Y. Ding, C. Manzo, G. Fulcrand, F. Leng, D. Dunlap, and L. Finzi, DNA supercoiling: A regulatory signal for the λ repressor, Proc. Natl. Acad. Sci. USA **111**, 15402 (2014).
[13] S. C. Dillon and C. J. Dorman, Bacterial nucleoid-associated proteins, nucleoid structure and gene expression, Nat. Rev. Microbiol. **8**, 185 (2010).
[14] J. F. Marko and E. D. Siggia, Statistical mechanics of supercoiled DNA, Phys. Rev. E **52**, 2912 (1995).
[15] J. F. Marko, Torque and dynamics of linking number relaxation in stretched supercoiled DNA, Phys. Rev. E **76**, 021926 (2007).
[16] A. V. Vologodskii, V. V. Anshelevich, A. V. Lukashin, and M. D. Frank-Kamenetskii, Statistical mechanics of supercoils and the torsional stiffness of the DNA double helix, Nature (London) **280**, 294 (1979).
[17] K. V. Klenin, A. V. Vologodskii, V. V. Anshelevich, A. M. Dykhne, and M. D. Frank-Kamenetskii, Computer simulation of DNA supercoiling, J. Mol. Biol. **217**, 413 (1991).
[18] A. V. Vologodskii, S. D. Levene, K. V. Klenin, M. Frank-Kamenetskii, and N. R. Cozzarelli, Conformational and thermodynamic properties of supercoiled DNA, J. Mol. Biol. **227**, 1224 (1992).
[19] J. F. Marko and E. D. Siggia, Bending and twisting elasticity of DNA, Macromolecules **27**, 981 (1994).
[20] T. R. Strick, J. F. Allemand, D. Bensimon, A. Bensimon, and V. Croquette, The elasticity of a single supercoiled DNA molecule, Science **271**, 1835 (1996).
[21] S. Forth, C. Deufel, M. Y. Sheinin, B. Daniels, J. P. Sethna, and M. D. Wang, Abrupt Buckling Transition Observed During the Plectoneme Formation of Individual DNA Molecules, Phys. Rev. Lett. **100**, 148301 (2008).
[22] H. Wada and R. R. Netz, Plectoneme creation reduces the rotational friction of a polymer, Europhys. Lett. **87**, 38001 (2009).
[23] J. F. Marko and S. Neukirch, Global force-torque phase diagram for the DNA double helix: Structural transitions, triple points, and collapsed plectonemes, Phys. Rev. E **88**, 062722 (2013).
[24] S. Neukirch and J. F. Marko, Analytical Description of Extension, Torque, and Supercoiling Radius of a Stretched Twisted DNA, Phys. Rev. Lett. **106**, 138104 (2011).
[25] M. van Loenhout, M. de Grunt, and C. Dekker, Dynamics of DNA supercoils, Science **338**, 94 (2012).
[26] F. C. Oberstrass, L. E. Fernandes, and Z. Bryant, Torque measurements reveal sequence-specific cooperative transitions in supercoiled DNA, Proc. Natl. Acad. Sci. USA **109**, 6106 (2012).
[27] T. Lepage, F. Képès, and I. Junier, Thermodynamics of long supercoiled molecules: insights from highly efficient Monte Carlo simulations, Biophys. J. **109**, 135 (2015).
[28] A. Fathizadeh, H. Schiessel, and M. R. Ejtehadi, Molecular dynamics simulation of supercoiled DNA rings, Macromolecules **48**, 164 (2015).
[29] F. Benedetti, A. Japaridze, J. Dorier, D. Racko, R. Kwapich, Y. Burnier, G. Dietler, and A. Stasiak, Effects of physiological self-crowding of DNA on shape and biological properties of DNA molecules with various levels of supercoiling, Nucleic Acids Res. **43**, 2390 (2015).
[30] C. Matek, T. E. Ouldridge, J. P. K. Doye, and A. A. Louis, Plectoneme tip bubbles: coupled denaturation and writhing in supercoiled DNA, Sci. Rep. **5**, 7655 (2015).
[31] I. D. Ivenso and T. D. Lillian, Simulation of DNA supercoil relaxation, Biophys. J. **110**, 2176 (2016).
[32] C. Barde, N. Destainville, and M. Manghi, Energy required to pinch a DNA plectoneme, Phys. Rev. E **97**, 032412 (2018).
[33] Y. A. Fosado, D. Michieletto, C. A. Brackley, and D. Marenduzzo, Nonequilibrium dynamics and action at a distance in transcriptionally driven DNA supercoiling, Proc. Natl. Acad. Sci. USA **118**, e1905215118 (2021).
[34] K. Ott, L. Martini, J. Lipfert, and U. Gerland, Dynamics of the buckling transition in double-stranded DNA and RNA, Biophys. J. **118**, 1690 (2020).
[35] I. De Vlaminck and C. Dekker, Recent advances in magnetic tweezers, Annu. Rev. Biophys. **41**, 453 (2012).
[36] J. Lipfert, M. Wiggin, J. W. J. Kerssemakers, F. Pedaci, and N. H. Dekker, Freely orbiting magnetic tweezers to directly monitor changes in the twist of nucleic acids, Nat. Commun. **2**, 439 (2011).
[37] W. Vanderlinden, E. Skoruppa, P. Kolbeck, E. Carlon, and J. Lipfert, DNA fluctuations reveal the size and dynamics of topological domains, bioRxiv, https://doi.org/10.1101/2021.12.21.473646.
[38] J. F. Marko and S. Neukirch, Competition between curls and plectonemes near the buckling transition of stretched supercoiled DNA, Phys. Rev. E **85**, 011908 (2012).
[39] M. Emanuel, G. Lanzani, and H. Schiessel, Multiplectoneme phase of double-stranded DNA under torsion, Phys. Rev. E **88**, 022706 (2013).
[40] J. D. Moroz and P. Nelson, Torsional directed walks, entropic elasticity, and DNA twist stiffness, Proc. Natl. Acad. Sci. USA **94**, 14418 (1997).
[41] J. F. Marko and E. D. Siggia, Stretching DNA, Macromolecules **28**, 8759 (1995).
[42] J. D. Moroz and P. Nelson, Entropic elasticity of twist-storing polymers, Macromolecules **31**, 6333 (1998).
[43] E. Skoruppa, M. Laleman, S. K. Nomidis, and E. Carlon, DNA elasticity from coarse-grained simulations: The effect of groove asymmetry, J. Chem. Phys. **146**, 214902 (2017).
[44] E. Skoruppa, S. K. Nomidis, J. F. Marko, and E. Carlon, Bend-Induced Twist Waves and the Structure of Nucleosomal DNA, Phys. Rev. Lett. **121**, 088101 (2018).
[45] E. Skoruppa, A. Voorspoels, J. Vreede, and E. Carlon, Length-scale-dependent elasticity in DNA from coarse-grained and all-atom models, Phys. Rev. E **103**, 042408 (2021).
[46] C. Bouchiat and M. Mézard, Elasticity Model of a Supercoiled DNA Molecule, Phys. Rev. Lett. **80**, 1556 (1998).
[47] C. Bouchiat and M. Mézard, Elastic rod model of a supercoiled DNA molecule, Eur. Phys. J. E **2**, 377 (2000).
[48] X. Gao, Y. Hong, F. Ye, J. T. Inman, and M. D. Wang, Torsional Stiffness of Extended and Plectonemic DNA, Phys. Rev. Lett. **127**, 028101 (2021).
[49] V. V. Rybenkov, N. R. Cozzarelli, and A. V. Vologodskii, Probability of DNA knotting and the effective diameter of the DNA double helix, Proc. Natl. Acad. Sci. USA **90**, 5307 (1993).
[50] D. Frenkel and B. Smit, *Understanding Molecular Simulation: From Algorithms to Applications*, 2nd ed., Computational Science Series Vol. 1 (Academic, San Diego, 2002).

[51] S. Kumar, J. M. Rosenberg, D. Bouzida, R. H. Swendsen, and P. A. Kollman, The weighted histogram analysis method for free-energy calculations on biomolecules. I. The method, J. Comput. Chem. **13**, 1011 (1992).

[52] Z. Liu and H. S. Chan, Efficient chain moves for Monte Carlo simulations of a wormlike DNA model: Excluded volume, supercoils, site juxtapositions, knots, and comparisons with random-flight and lattice models, J. Chem. Phys. **128**, 145104 (2008).

[53] L. Coronel, A. Suma, and C. Micheletti, Dynamics of supercoiled DNA with complex knots: large-scale rearrangements and persistent multi-strand interlocking, Nucleic Acids Res. **46**, 7533 (2018).

[54] S. K. Nomidis, E. Skoruppa, E. Carlon, and J. F. Marko, Twist-bend coupling and the statistical mechanics of the twistable wormlike-chain model of DNA: Perturbation theory and beyond, Phys. Rev. E **99**, 032414 (2019).

[55] M. Caraglio, E. Skoruppa, and E. Carlon, Overtwisting induces polygonal shapes in bent DNA, J. Chem. Phys. **150**, 135101 (2019).

[56] A. V. Vologodskii and J. F. Marko, Extension of torsionally stressed DNA by external force, Biophys. J. **73**, 123 (1997).

[57] Z. Yang, Z. Haijun, and O. Y. Zhong-Can, Monte Carlo implementation of supercoiled double-stranded DNA, Biophys. J. **78**, 1979 (2000).

[58] C. Maffeo, J. Yoo, J. Comer, D. Wells, B. Luan, and A. Aksimentiev, Close encounters with DNA, J. Phys.: Condens. Matter **26**, 413101 (2014).

[59] P. R. Desai, S. Brahmachari, J. F. Marko, S. Das, and K. C. Neuman, Coarse-grained modelling of DNA plectoneme pinning in the presence of base-pair mismatches, Nucleic Acids Res. **48**, 10713 (2020).

[60] J. F. Marko, Biophysics of protein-DNA interactions and chromosome organization, Phys. A (Amsterdam) **418**, 126 (2015).

[61] We remark that writhe is technically only defined for a closed space curve, which in the context of stretched linear DNA is usually resolved by introducing a virtual closure either at infinity or through a large arc [56,64]. We ignore these closure contributions, since they are irrelevant for the detection of plectonemes.

[62] K. Klenin and J. Langowski, Computation of writhe in modeling of supercoiled DNA, Biopolymers **54**, 307 (2000).

[63] S. K. Nomidis, Theory and simulation of DNA mechanics and hybridization, Ph.D. thesis, KU Leuven, 2020.

[64] F.-C. Chou, J. Lipfert, and R. Das, Blind predictions of DNA and RNA tweezers experiments with force and torque, PLoS Comput. Biol. **10**, e1003756 (2014).